The Journal of Chemical Physics

RESEARCH ARTICLE | AUGUST 21 2024

Morphological control of bundled actin networks subject to fixed-mass depletion

James Clarke ; Lauren Melcher; Anne D. Crowell ; Francis Cavanna ; Justin R. Houser; Kristin Graham ; Allison M. Green ; Jeanne C. Stachowiak; Thomas M. Truskett ; Delia J. Milliron ; Adrianne M. Rosales ; Moumita Das ; José Alvarado

J. Chem. Phys. 161, 074905 (2024)
https://doi.org/10.1063/5.0197269

AIP Publishing

The Journal of Chemical Physics ARTICLE pubs.aip.org/aip/jcp

Morphological control of bundled actin networks subject to fixed-mass depletion

Cite as: J. Chem. Phys. 161, 074905 (2024); doi: 10.1063/5.0197269
Submitted: 12 January 2024 • Accepted: 10 July 2024 •
Published Online: 21 August 2024

James Clarke,[1] Lauren Melcher,[2] Anne D. Crowell,[3] Francis Cavanna,[1] Justin R. Houser,[4] Kristin Graham,[4] Allison M. Green,[3] Jeanne C. Stachowiak,[3,4] Thomas M. Truskett,[3] Delia J. Milliron,[3] Adrianne M. Rosales,[3] Moumita Das,[2,5] and José Alvarado[1,a)]

AFFILIATIONS

[1] UT Austin Department of Physics, 2515 Speedway, Austin, Texas 78712, USA
[2] School of Mathematical Sciences, Rochester Institute of Technology, Rochester, New York 14623, USA
[3] UT Austin McKetta Department of Chemical Engineering, E 24th St., Austin, Texas 78712, USA
[4] UT Austin Department of Biomedical Engineering, Austin, Texas 78712, USA
[5] School of Physics and Astronomy, Rochester Institute of Technology, Rochester, New York 14623, USA

[a)] **Author to whom correspondence should be addressed:** alv@chaos.utexas.edu

ABSTRACT

Depletion interactions are thought to significantly contribute to the organization of intracellular structures in the crowded cytosol. The strength of depletion interactions depends on physical parameters such as the depletant number density and the depletant size ratio. Cells are known to dynamically regulate these two parameters by varying the copy number of proteins of a wide distribution of sizes. However, mammalian cells are also known to keep the total protein mass density remarkably constant, to within 0.5% throughout the cell cycle. We thus ask how the strength of depletion interactions varies when the total depletant mass is held fixed, a.k.a. fixed-mass depletion. We answer this question via scaling arguments, as well as by studying depletion effects on networks of reconstituted semiflexible actin *in silico* and *in vitro*. We examine the maximum strength of the depletion interaction potential U^* as a function of q, the size ratio between the depletant and the matter being depleted. We uncover a scaling relation $U^* \sim q^{\zeta}$ for two cases: fixed volume fraction φ and fixed mass density ρ. For fixed volume fraction, we report $\zeta < 0$. For the fixed mass density case, we report $\zeta > 0$, which suggests that the depletion interaction strength increases as the depletant size ratio is increased. To test this prediction, we prepared our filament networks at fixed mass concentrations with varying sizes of the depletant molecule poly(ethylene glycol) (PEG). We characterize the depletion interaction strength in our simulations via the mesh size. In experiments, we observe two distinct actin network morphologies, which we call weakly bundled and strongly bundled. We identify a mass concentration where different PEG depletant sizes lead to weakly bundled or strongly bundled morphologies. For these conditions, we find that the mesh size and intra-bundle spacing between filaments across the different morphologies do not show significant differences, while the dynamic light scattering relaxation time and storage modulus between the two states do show significant differences. Our results demonstrate the ability to tune actin network morphology and mechanics by controlling depletant size and give insights into depletion interaction mechanisms under the fixed-depletant-mass constraint relevant to living cells.

INTRODUCTION

The intracellular cytosol is a crowded environment with a high concentration of soluble proteins. Many kinds of intermolecular interactions, such as van-der-Waals, electrostatic, and hydrophobic interactions, ultimately determine the protein structure, binding, and function. In addition, steric effects play a significant role and contribute to intermolecular interactions in complex ways: they mediate short-range repulsion, promote nematic alignment and defects, and mediate interactions with boundaries and confining geometries.[1] Strikingly, a crowded solution of small depletant molecules can, through steric repulsion, drive short-ranged attractive interactions (depletion interactions) between larger, micrometer-scale structures.[2] Depletion interactions from

intracellular proteins are thus believed to contribute to the spatial organization of intracellular structures such as the nucleus, amyloid fibrils, and the cytoskeleton.[3] However, quantifying how depletion interactions contribute to intracellular organization remains a challenging task, given the large number of short-ranged steric interactions and complex spatial hierarchy in living cells.

Although depletion in living cells remains difficult to characterize, researchers have successfully studied depletion in a wide range of model systems: colloids,[4] polymer-coated nanocrystals,[5] actively stirred rods and beads,[6] actin and DNA polymers in solutions,[7] DNA polymers suspended with increasing sizes of dextran molecules,[8] and microtubules driven by poly(ethylene glycol) (PEG) polymers.[9] These studies have found that the maximum strength of the depletion interaction U^* at close contact scales with the overlap volume $V_{overlap}$, that is, the additional volume made available to the depletants when the colloids are in close contact. It has been well established that increasing depletant concentration generally increases the depletion interaction strength and increasing depletant size generally increases the depletion interaction length scale. This has been determined typically by performing many experiments that systematically vary depletant concentration and depletant size.

However, cells are not thought to significantly vary protein concentration. In fact, mammalian cells have been recently shown to keep the total protein mass density remarkably constant, to within 0.5% throughout the cell cycle.[10] Instead, cells dynamically regulate the copy number of proteins over a wide distribution of sizes. This raises the following question: how are depletion interactions affected when the total depletant mass is held fixed but the depletant size is allowed to vary? That is, what is $U^*(q)$ for fixed mass density ρ? Here, q is the size ratio between the depletant and the matter being depleted. Surprisingly, however, prior studies on depletion interactions do not appear to provide a clear answer to this question. One reason for this is that depletant concentration can be given in terms of number density, volume fraction, or mass density. These three quantities may appear to be roughly equivalent measures and are often taken to be interchangeable. Another reason is that, experimentally, varying depletant concentration or depletant size *in situ* remains technically challenging. Answering this question is essential to better understand how steric repulsion and depletion interactions contribute to intracellular structures in crowded environments. In addition, understanding and characterizing fixed-mass depletion could be leveraged to develop novel biomimetic materials. Control over depletant size distribution could be a useful experimental knob for affecting interactions, structure, and mechanics of novel materials for biomedical or soft-robotics applications without requiring direct covalent or specific interactions between constituent polymers or colloids.

In order to study fixed-mass depletion, we turn to a combination of scaling arguments, simulations, and experiments that utilize an *in vitro* model system of actin biopolymers and PEG polymers as depletants. Actin is one of the most prevalent biopolymers in the cell and a key component driving mechanics in the cellular cortex. It exhibits a wide polymorphism in its ability to polymerize and then form higher-order structures out of the polymerized actin.[11] Of specific interest for the work presented herein are actin bundles, which are utilized in lamellipodia,[12] filopodia,[11] stress fibers,[13] and microvilli.[14] The mechanisms driving bundle formation are varied, and several have been identified *in vitro*. Electrostatic bundling via counterion condensation screens charges held on the actin and, by electric attraction, pulls actin filaments into bundles.[15–17] Physiological bundling depends on specific proteins that are known to specifically bind to and cross-link actin,[18] such as fascin,[19] α-actinin,[20] and filamin.[21,22] Bundle formation can also be caused by the depletion interaction. Above a threshold concentration of depletant molecules, individual actin filaments self-bundle into rings and raquets,[23] and more concentrated networks of actin filaments form networks of entangled bundles.[24,25]

We consider ideal PEG polymers to investigate how the strength of depletion interactions varies as depletant size varies under fixed mass constraints. The relationship between depletant size and mass is characterized by the Flory exponent ν.[26] Although the Flory exponent of ideal PEG polymers in a good solvent ($\nu = 3/5$) differs from that of most proteins (ν in the range 1/3–2/5; see Discussion and work by Minton[27]), we choose to use PEG because prior studies have already established it as a bundling agent via depletion interactions, and PEG has an easily tunable molecular weight.[24,28] Therefore, to explore this connection, we investigate PEG as a model system for depletion interactions mediated by sterically interacting proteins in a crowded intracellular environment. In the second half of this work, we characterize two distinct states of our system, Γ_{6k} and Γ_{20k}, which demonstrate a large change in morphology when depletant mass distribution is changed slightly from 6 to 20 kDa under the fixed-mass constraint. In particular, structural measures such as the mesh size, the spacing between bundles, the relaxation time of the network, and the bulk mechanical properties of the network are investigated.

RESULTS

Analytical scaling arguments: Fixed-volume vs fixed-mass constraints

We begin by developing an analytical framework to investigate fixed-mass depletion. In order to understand how the strength of the depletion interaction varies while depletant mass is held fixed, we examine here the seminal Asakura–Oosawa model[29] for two cases: fixed volume fraction φ and fixed mass density ρ. We first consider two colloidal spheres of fixed diameter σ, immersed in a solution containing spherical depletants (e.g., polymers) with variable diameter τ and variable number density n. The interaction potential U between the two colloidal spheres is given by

$$U(d) = -nkTV_{overlap}(d), \quad d \le 1, \tag{1}$$

where k is the Boltzmann constant, T is the temperature, $V_{overlap} = \frac{\pi}{6}\sigma^3(1+q)^3\left(1-\frac{3}{2}d+\frac{1}{2}d^3\right)$ is the overlap volume,[30] D is the distance between the two colloids' center of masses, $d = \frac{D}{\sigma(1+q)}$ is the distance normalized by the maximal extent of the depletion interaction, and $q = \frac{\tau}{\sigma}$ is the size ratio. We wish to determine the maximal value U^* of the interaction potential, which occurs when the two colloids are in contact and thus $D = \sigma$, or equivalently $d = \frac{1}{1+q}$. Furthermore, we wish to determine how the scaling relation $U^* \sim q^{\zeta}$ is affected by the two cases of fixed φ and fixed ρ.

We now consider the above expressions for the scenario where the depletant is much smaller than the colloids. We only consider the values of q smaller than 0.1547 because the Asakura–Oosawa

(AO) model tends to break down at higher values of q.[30] While only exact in this range, we note that previous studies have shown AO theory to be a viable approximation for larger values of q.[31,32] In the considered regime, we note that the right-hand factor containing the third-order polynomial in d in the above expression for $V_{overlap}$ Taylor expands to scale as q^2, yielding $V_{overlap} \sim \sigma^3(1+q)^3q^2$. For the fixed volume fraction case, we have $\varphi = \frac{4}{3}\pi\left(\frac{\tau}{2}\right)^3 n$. Substituting into the above equation for $U(d)$ yields $U^* \sim -\varphi\left(\frac{1+q}{q}\right)^3 q^2 \sim q^{-1}$. The negative scaling exponent $q^\zeta \equiv q^{-1}$ tells us that breaking up a fixed volume of spherical depletants into smaller spheres increases the number density to allow the interaction potential to diverge as $q \to 0$. Thus, for fixed volume fraction, smaller depletants result in stronger depletion interactions.

In contrast, for the fixed mass density case, we have $\rho = MW\ n \sim R_g^{\frac{5}{3}} n$, where we use the Flory scaling relation for polymers.[26] Substituting into the above equation for $U(d)$ produces a positive scaling exponent ζ,

$$U^* \sim -\rho\sigma^{\frac{4}{3}}\frac{(1+q)^3}{q^{5/3}}q^2 \sim q^{\frac{1}{3}}. \tag{2}$$

This relation predicts that two colloidal spheres will experience a stronger attractive interaction if polymer depletants become larger while maintaining the mass density fixed.[30]

To extend this analysis to actin, we turn to the case where we consider two cylindrical rods to better approximate actin filaments. The maximum depletion interaction potential between a pair of non-parallel cylindrical rods of cross-sectional diameter σ is given by $\frac{U^*}{kT} = -\frac{\pi}{2}n\sigma\tau^2 = -\frac{\pi}{2}nq^{-1}\tau^3$.[33] Thus, at fixed volume fraction, we have $\varphi = \frac{4}{3}\pi\left(\frac{\tau}{2}\right)^3 n$, which gives an interaction potential $\frac{U^*}{kT} = -3\varphi q^{-1}$.

Here, we observe a negative scaling exponent $\zeta = -1$ as before. For the fixed mass density case, we have $\rho = M_W n \sim \tau^{\frac{5}{3}} n$, whose associated interaction potential is given by

$$\frac{U^*}{kT} = -\frac{\pi}{2}\sigma^{\frac{4}{3}}\rho q^{\frac{1}{3}}, \tag{3}$$

with $q = \frac{\tau}{\sigma}$ as defined earlier. We observe the same positive scaling exponent $\zeta = \frac{1}{3}$ in the interaction potential as obtained for the pair of spheres described above.

Furthermore, for the case of parallel cylinders, with interaction potential $\frac{U^*}{kT} = -\frac{2\sqrt{2}}{3}Ln\tau^{\frac{3}{2}}\sigma^{\frac{1}{2}}$,[33] we obtain

$$\frac{U^*}{kT} = -\frac{4}{\pi}L\sigma^{-1}q^{\frac{-3}{2}} \tag{4}$$

for the case of fixed volume fraction and

$$\frac{U^*}{kT} = -\frac{2\sqrt{2}}{\pi}L\sigma^{\frac{2}{3}}q^{\frac{1}{6}} \tag{5}$$

for the case of fixed mass density. With parallel cylinders, we get different scaling relationships of $\frac{U^*}{kT}$ with q but obtain a similar reversal of sign of the scaling exponent ζ as was observed for the case of spherical particles and non-parallel cylinders. Namely, the interaction potential decreases with q for fixed volume fraction and increases with q for fixed mass density.

Note that these relationships only hold when $\frac{\pi n\tau^3}{6} \ll 1$. For very dense systems where this condition is violated, we can apply Carnahan–Starling theory such that the number density of depletants n should be replaced by nZ, where $Z = \frac{1+\eta+\eta^2-\eta^3}{(1-\eta)^2}$, in which $\eta = \frac{\pi n\tau^3}{6}$.[33] For a fixed volume fraction φ, $Z = \frac{1+\varphi+\varphi^2-\varphi^3}{(1-\varphi)^2}$, i.e., there is no change to the scaling of $\frac{U^*}{kT}$ with q. However, for a fixed mass density, $Z = 1 + \frac{1}{2}\pi\rho\sigma^{\frac{4}{3}}q^{\frac{4}{3}} +$ higher order terms, which will change the scaling when $q \sim 1$.

Given these results, we hypothesize that the depletion interaction strength increases as the depletant size is increased, subject to the constraint that mass is held fixed. In order to test this hypothesis, we turn to numerical simulations.

Validation via simulation: Larger depletants increase actin bundling

To investigate the underlying depletion mechanism for fixed depletant mass systems, we developed a numerical model, which consists of actin filaments interacting with spherical PEG particles in three dimensions. Actin filaments are long compared to the PEG molecules. The persistence length of actin is 17 μm,[34,35] and the diameter of F-actin is about 7–8 nm.[36,37] The radius of gyration for PEG is given by $R_g \sim MW^{3/5}$.[26] In this section, we examine PEGs with R_g both smaller and larger than the diameter of F-actin. Given the difference in length scales and sufficient concentrations of PEG, there is an entropic favorability for PEG to occupy maximal volume. PEG accomplishes this by depleting the distances between actin filaments in its local environment, thus inducing bundle formation. When two filaments are closer than twice the radius of a PEG molecule, the filaments act as a semi-permeable structure where fluid is permitted to flow, but PEG particles are excluded from the region. This attracts the two filaments toward one another, effectively depleting any separation between them.[38]

To model this type of interaction numerically, each actin filament is modeled as a chain made of beads, and the relative cost of stretching and bending the chain is informed by the known mechanical properties of actin filaments. We model the pairwise interactions between any two particles, whether belonging to actin bead-chains, or PEG, or between actin and PEG using a Lennard-Jones potential, $V_{LJ} = 4\varepsilon\left[12\frac{\sigma_{ab}^{12}}{r_{ij}^{13}} - 6\frac{\sigma_{ab}^{6}}{r_{ij}^{7}}\right]$, where $\sigma_{ab} = \frac{\sigma_a+\sigma_b}{2}$, in which σ_a and σ_b represent the diameters of two reference beads. The interparticle distance between two reference particles with indices i and j is denoted by r_{ij}, and the strength of the interaction's potential is defined by ε. The interaction potential is truncated to incorporate only repulsive interactions representing a hard core for actin–PEG interactions giving the Weeks–Chandler–Anderson potential,[39] while for PEG–PEG and actin–actin interactions, we additionally allow attractive interactions to mimic the van der Waals interactions.

The motion of the PEG particles follows the overdamped Langevin equation, $\frac{dr}{dt} = \frac{D}{kT}F_{LJ} + \sqrt{2D}\eta$, where the interparticle interaction force F_{LJ} is derived from the Lennard-Jones potential defined above, and the thermal diffusion is represented by the noise term $\sqrt{2D}\eta$, where D is the diffusion constant and η is a vector

drawn from a Gaussian distribution with a mean of 0 and variance of 1; k and T are the Boltzmann constant and room temperature. The motion of an actin bead in strand i is also given by an overdamped Langevin equation: $\frac{dr_i}{dt} = \frac{D}{kT}\left(\sum F_{LJ_{ij}} + \sum F_{LJ_{ik}} + \sum F_{LJ_{il}}\right) + \frac{D}{kT}\left(\sum F_{s,ij} + \sum F_{b,ij}\right) + \sqrt{2D}\eta$, where $F_{LJ_{ij}}$, $F_{LJ_{ik}}$, and $F_{LJ_{il}}$ are the Lennard-Jones interparticle forces, and the indices i and j describe intra-strand pairwise interactions, i and k describe inter-strand interactions, and i and l describe interactions between actin and PEG particles. The actin filaments resist stretching (or compression) and bending with forces $F_{s,ij}$ and $F_{b,ij}$, respectively, obtained from the corresponding stretching and bending deformation energies, $U_s = \frac{K_s}{2}(l - l_0)^2$ and $U_b = \frac{K_b}{2}(\theta - \theta_0)^2$. In these equations, l represents the distance between two nearest-neighbor actin beads in a strand and l_0 describes the equilibrium rest length for actin beads, which is given by the actin bead diameter. The stretching stiffness is K_s, the bending rigidity is K_b, and θ is the angle between three sequential actin beads, and the equilibrium value of this angle, θ_0, is set to π.

We solve both Langevin equations using the forward Euler–Maruyama approach. The time step dt is set to $10^{-3}\tau$, and each simulation was run up to 500 τ or 50 s. In our simulations, this time was sufficient for the system to reach a long-lived steady state, where the average mesh size remained steady. This was confirmed by monitoring the system configurations in longer runs in some of our simulations. This run time of ~50 s is approximately an order of magnitude smaller than typical experimental run times. However, given that the simulated actin filaments are 160 nm long compared to the experimental values of several micrometers, we believe that our simulated morphologies likely reached steady states more quickly than in experiments. Nevertheless, we cannot rule out the potential for this to cause some discrepancy in the self-assembly dynamics and steady state morphologies between the simulations and experiments.

The simulation results are shown in Fig. 1. With our model, we present two sets of simulation cases. In the first case, we vary both the radii of the PEGs and the number density of PEGs [Fig. 1(a)]. In a second set of simulations, the PEG mass density is kept constant and the radii of gyration range from 4 to 20 nm [Fig. 1(b)].

To explore the trade-off associated with holding the total depletant mass fixed, while varying the size of the depletant, we select three radii of interest $R_{g,1}$, $R_{g,2}$, and $R_{g,3}$ that correspond to ~4, 8, and 20 nm PEGs. The simulation depletant sizes were chosen to explore a large q regime. For $R_{g,1}$, the number of PEG molecules was set to 6000, $R_{g,2}$ had a total of 1890 PEG molecules, and $R_{g,3}$ had a total of 410 PEG molecules, to keep the mass density fixed. These correspond to PEGs of MW ~20, ~70, and ~317 kDa. Statistical results corresponding to depletion interactions simulated for these different cases are shown in Fig. 1(b).

The results of Fig. 1(b) are qualitatively consistent with our predictions from the scaling arguments presented in the section on Analytical scaling arguments: Fixed-volume vs fixed-mass constraints, as we see a steady increase in the network mesh size as a result of increasing the PEG molecular weight at fixed mass density. We take the mesh size, ξ, to directly reflect differences in U^* because increases in mesh size correspond to more effective bundling in the system[40] and thus a stronger interaction potential (see Figs. S1 and S2). Details on the mesh size algorithm can be found in the supplementary material (Fig. S1). Given the simulation results, we decided to test if the numerically supported scaling predictions extend to the same system studied *in vitro*.

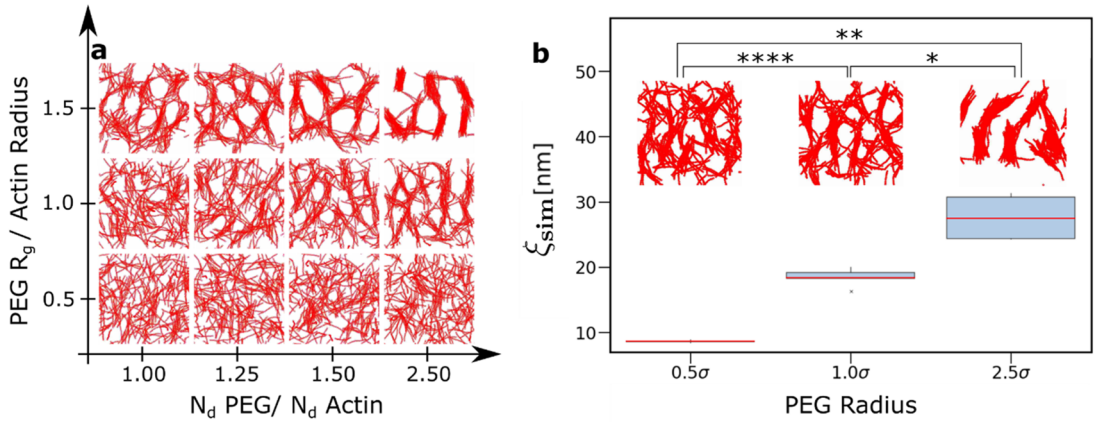

FIG. 1. (a) Simulation snapshots showing the simulated long-time steady-state morphologies of the networks and bundles of actin filaments in the presence of PEG. These snapshots demonstrate the role of PEG molecular weight and concentration on the actin filament bundling. As the molecular weight, and thus size ratio q, increases (y-axis), significant bundling of actin filaments is observed. Similarly, increasing the number density, N_d, of PEG (x-axis) also leads to appreciably more pronounced bundles. R_g is the radius of gyration for a given PEG molecule, where $R_g \sim MW^{3/5}$. (b) Box plots presenting the mesh size of simulated actin gels when PEG size is varied while keeping the total mass of PEG in the system fixed, i.e., reducing N_d of PEG when increasing molecular weight ($N = 5$ simulations). The inset tiles are real space representations of network morphology for the corresponding distribution directly below them. For interpreting the box plots, the top and bottom of each box give the upper and lower quartiles where the box height represents 50% of the distribution, the lines above and below the box represent the upper and lower whiskers where the distance between them represents 100% of the distribution, and the red line inside the box indicates the median value. $\sigma = 8$ nm.

Validation via experiment: Larger depletants increase actin bundling

Given the predictions made from the modeling, we moved to study these systems with *in vitro* experimental assays. Bundled actin networks were assembled (see Methods) and subsequently imaged with a confocal microscope. We study PEGs of variable molecular weight and size: for 20 kDa, $R_g \simeq 3.9$ nm; for PEG 6 kDa, $R_g \simeq 1.9$ nm; and for PEG 2 kDa, $R_g \simeq 0.9$ nm.[26] The primary results of this section are captured in Fig. 2. Figure 2(a) shows confocal micrographs of fluorescently tagged actin filaments that capture our experimental parameter space, representing 36 distinct samples to give three replicates per sample condition. For a representation of Fig. 2(a) in number density space, see Fig. S3 of the supplementary material. Figure 2(b) shows the results of our mesh size analysis performed on the data represented in Fig. 2(a).

We find qualitative agreement between the configuration space diagram produced by the simulation [cf. Fig. 1(a)] and that of experiment Fig. 2(a). In both simulation and experiment, the actin network exhibits increased bundling as either PEG concentration or PEG molecular weight is increased. However, the way the system changes to a purely bundled state appears to be more abrupt in the experiment than in simulation (see Discussion). Furthermore, we note that we do see statistically significant differences in mesh size among the 1.0 wt. %/vol. % assays. This result lends experimental support to our earlier hypothesis from the simple scaling model, as well as our observed trend in simulations [cf. Fig. 1(b)].

We also observe two morphologically distinct regions of actin networks by systematically varying the molecular weight and concentration of PEG molecules in the assay. In Fig. 2(a), one can observe a distinction between weakly bundled and strongly bundled networks to the left and right of the blue line in Fig. 2, respectively. In the weakly bundled regime, the coexistence of actin bundles and single-filament actin networks is observed, whereas for strongly bundled samples, a network of actin bundles is formed. To quantify the regions between weakly bundled and strongly bundled networks, we developed a separate image processing algorithm, the degree of bundling, which quantifies the presence of bundles and hence the observed morphologies (see the supplementary material). We find that strongly bundled networks occur for a degree of bundling greater than ~0.2 (a.u.) (Fig. S4). Figure 2(b) demonstrates that we observe increasing bundling strength as we increase the PEG concentration, as well as for increasing PEG molecular weight. Finally, we note that although the actin filaments in the simulation (≈160 nm in length) are much smaller than in experiment (~several micrometers), the mesh sizes in the simulations range from ~1/16 to 1/5 of the actin filament length [Fig. 1(b)]. This ratio is comparable to that observed in experiments, where we found the mesh size [cf. Fig. 2(b)] to be between 1/10 and 1/2, assuming an average filament length of 5 μm (Fig. S5). The comparability of these two ratios suggests that similar physics underlies the behavior found in simulation and experiment, despite differences in absolute scale. In all, we take the experimental results of Fig. 2 to be in qualitative agreement with our earlier analytical and numerical predictions.

In the remaining parts of the Results section, we characterize microscopic and bulk properties of two conditions. When we vary q, we observe the most dramatic change in morphology between PEG MWs 6k and 20k at [PEG] = 0.1% (w/v), which we refer to as

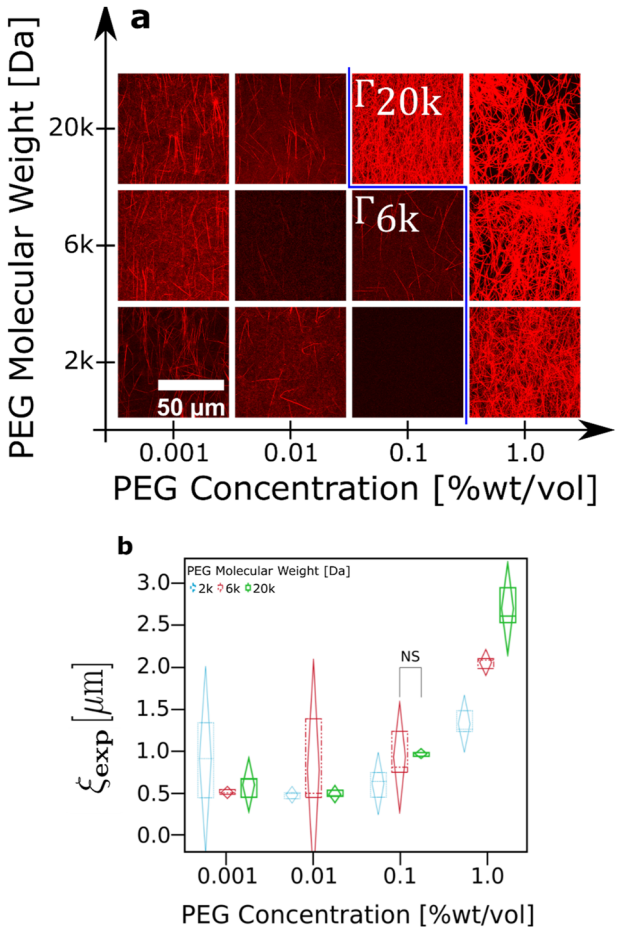

FIG. 2. (a) A representative phase diagram of [actin] = 12 μM with various concentrations (wt. %/vol. %) of PEG on the x-axis and the molecular weight of the PEG on the y-axis corresponding to a total of 36 distinct samples, giving three replicates for each condition. Scale bar = 50 μm. The threshold concentration of bundling (blue line) for PEG 6k and PEG 2k is at [PEG] = 1.0% (w/v), and for PEG 20k at [PEG] = 0.1% (w/v). Γ_{6k} and Γ_{20k} denote the regions of interest for further characterization. Each tile represents a max intensity confocal z-projection across a 25.5 μm depth. (b) Quartile box plots with confidence diamonds of each network's mean mesh size in micrometers extracted from confocal micrographs for various concentrations of PEG ($N = 3$ experiments per each sample condition). The molecular weight of the PEG is given in the inset legend, where blue fine-dashes, red irregular-dashes, and green solid-line correspond to PEG at molecular weights of 2k, 6k, and 20k. A direct comparison is drawn between Γ_{6k} and Γ_{20k}, where we can see that the mesh size is statistically identical for the two populations. NS denotes that two populations are statistically indistinguishable. For interpreting the box plots, the top and bottom of each box give the upper and lower quartiles where the box height represents 50% of the distribution. The horizontal line inside the box indicates the median value of the distribution. The top and bottom of the diamond are a 95% confidence interval for the mean. The middle of the diamond is the sample average, which is an estimate of the population mean.

Γ_{6k} and Γ_{20k}, respectively. These points are shown in overlay in Fig. 2(a). We note that other regions of our parameter space were not studied further in favor of investigating the Γ_{6k} and Γ_{20k} conditions more thoroughly as we hypothesize that network properties will

be distinct and may be leveraged for soft material applications. In Fig. 2(b), we observe that the mesh size distributions for the Γ_{6k} and Γ_{20k} states are statistically indistinguishable from one another due to the large variance in the Γ_{6k} mesh size. This spread and its impact on proximity to significant separation are within our expectations for this system as these samples are located near different morphological regimes, weakly and strongly bundled, and are thus more sensitive to sample-to-sample variation. This variation manifests here in the mesh size distribution for Γ_{6k}. We begin the remaining materials characterization with an investigation into the dynamics of our actin gels using dynamic light scattering.

Material characterization: Diffusion of actin polymers in dynamic light scattering

To determine the diffusive properties of Γ_{20k}, Γ_{6k}, and a control without PEG, the samples were probed with a Zetasizer Nano ZS instrument, with a q-vector of $|q| = \frac{4\pi \cdot 1.334}{632\ \text{nm}} \sin(173°/2) = 26.4\ \mu\text{m}^{-1}$ (see Methods). This q-vector was chosen to set the scale of the dynamics probed within the network.[41] Correlation curves describing the timescale associated with the decorrelation of the system from an original scattering state for each condition measured with dynamic light scattering are represented (Fig. S6). The DLS correlation curves are fit using Eq. (3) (see Methods) to extract relevant parameters, such as relaxation time, τ_f, and stretch exponent, β. The results are shown in Fig. 3.

Actin–PEG systems polymerize on the order of tens of seconds, in contrast to systems that experience gelation over dozens of minutes.[42,43] Consequently, we observe no polymerization phase, and the plots represent the system at or close to a stabilized state. The relaxation time of the Γ_{20k} condition, $\tau_{f,20} = 2314 \pm 40\ \mu$s, is roughly twice that of the control condition, $\tau_f = 1053 \pm 3\ \mu$s, with the Γ_{6k} condition somewhere in between, at $\tau_{f,6} = 1833 \pm 22\ \mu$s. Relaxation time corresponds to the time needed for the intensity correlation function to decay. Longer times correspond to less diffusive networks, and shorter times correspond to networks undergoing more motion. In addition, fitting the correlation function yields the stretching exponent, β, which indicates how broad the relaxation times are. β is defined between 0 and 1, and $\beta = 1$ corresponds to a single relaxation time, while $\beta < 1$ corresponds to an increased broadening of relaxation times as β decreases to 0. The stretched exponential fits reveal that the Γ_{20k} condition has a lower stretching exponent β than that of Γ_{6k} and the control, which suggests a more heterogeneous distribution of relaxation timescales for the Γ_{20k} condition than the Γ_{6k} condition. Stretched exponent and relaxation time calculations have previously characterized the formation of colloidal gels[42] and precursors to contraction of active networks.[44]

Material characterization: Intra-bundle distance using FRET

The Γ_{6k} and Γ_{20k} states were also characterized using Förster Resonant Energy Transfer (FRET). FRET has been proposed as a sensing mechanism in a myriad of biochemical contexts[45] and utilized to study membrane crowding and steric pressure on membranes.[46,47] In this study, we utilized FRET as a sensor to measure the distribution in intra-bundle distances between neighboring actin filaments in our system, where perturbations in the fluorescent lifetime can be correlated with real-space distances between a donor and an acceptor.[48]

Using the fluorescence lifetimes measured in both Γ_{6k} and Γ_{20k}, τ_{DA}, along with the fluorescence lifetime of the sample without any acceptor fluorophores, τ_D, we calculate the FRET efficiency E as

$$E = 1 - \frac{\tau_{DA}}{\tau_D}. \tag{6}$$

Given that this is measured on a per-pixel basis, with spatial separation of 300 nm per pixel in the sample, the measured efficiency is built using the mean of the respective fluorescence lifetimes,

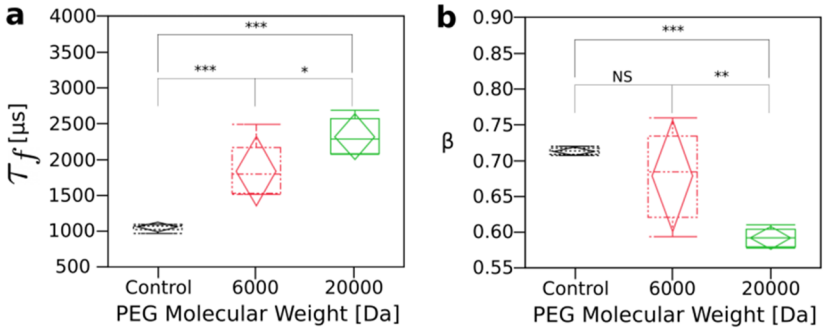

FIG. 3. Each DLS correlation curve (see Fig. S6) was fit, and a relaxation time, τ_f, and a stretch exponent, β, were obtained from the fit. The relaxation time for each condition is represented in (a) and was $\tau_{f,20} = 2314 \pm 40\ \mu$s, $\tau_{f,6} = 1833 \pm 22\ \mu$s, and $\tau_f = 1053 \pm 3\ \mu$s. The relaxation time for the Γ_{20k} condition was significantly different from the relaxation time for the Γ_{6k} condition ($p = 0.0166$), and the Γ_{6k} condition was significantly different from the state with no PEG ($p = 0.0007$). The stretch exponent is represented in (b) and is $\beta_{20} = 0.59 \pm 0.01$, $\beta_6 = 0.68 \pm 0.06$, and $\beta_c = 0.713 \pm 0.004$. The difference between relaxation times for the control and the Γ_{6k} condition is not significant ($p = 0.1668$), but the difference between the Γ_{6k} condition and the Γ_{20k} condition is significant ($p = 0.0030$). For interpreting the box plots, the top and bottom of each box give the upper and lower quartiles where the box height represents 50% of the distribution, and the horizontal lines above and below the box represent the upper and lower whiskers where the distance between them represents 100% of the distribution. The horizontal line inside the box indicates the median value of the distribution. The top and bottom of the diamond are a 95% confidence interval for the mean. The middle of the diamond is the sample average, which is an estimate of the population mean.

giving a spatially averaged efficiency, $\langle E \rangle$. With this, the average donor–acceptor distance is calculated using

$$R_{DA} = R_0 \left(\frac{1}{\langle E \rangle} - 1 \right)^{\frac{1}{6}}, \tag{7}$$

where R_0 is the Förster radius determined to be 6.72 nm by the choice of donor and acceptor in the system.[48]

The main result of the FRET analysis is that the intra-bundle spacing between filaments is statistically indistinguishable across our samples as demonstrated in Fig. 4.[49]

Material characterization: Bulk mechanical properties of bundled actin networks

Previous studies characterized the bulk rheological properties of actin networks bundled via physical cross-links, such as scruin[50,51] as well as with covalent cross-links.[52] The rheological properties of actin networks bundled via depletion forces have also been studied with respect to changes in PEG concentration.[28] As previously noted, however, the effect of PEG molecular weight on the bulk rheological properties of bundled actin networks has not been quantified. Thus, in this study, oscillatory shear rheometry is used to characterize the bulk properties of the bundled actin networks. Specifically, we measure the storage modulus (G') and loss modulus (G'') as a function of time for the Γ_{6k} and Γ_{20k} states (Fig. 5). G' is especially of interest because it provides a measure of the bulk elasticity of the networks. Three replicates of each network type were created in pairs: for each replicate, enough actin for two networks was prepared, and from this actin preparation, one Γ_{6k} sample and one Γ_{20k} sample were each formulated. This experimental design was then executed on two different geometries, parallel plate (PPG) and conical (CG). Figure 5(a) shows the evolution of G' and G'' over time for one of the CG replicates. G' increases during the first 10 min for both networks. Because the components of the network are mixed immediately before beginning measurements on the rheometer, the increase in G' during that period is attributed to the formation of the bundled actin networks, corresponding to the gelation time scale.[43] After this time, G' plateaus to a steady value, suggesting that network formation is complete. Although a previous report shows that the formation of actin

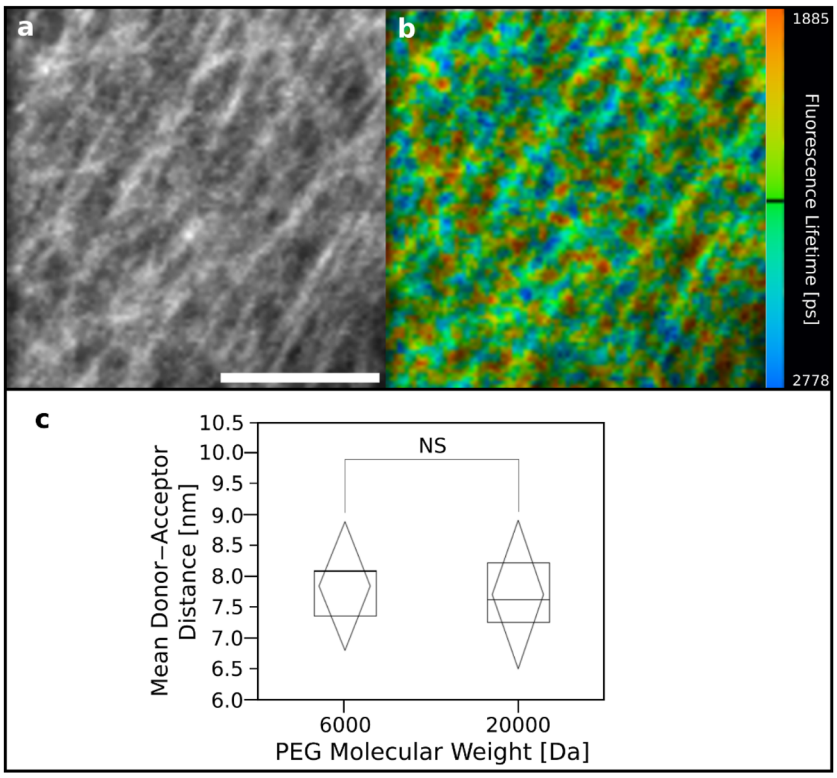

FIG. 4. (a) FRET intensity confocal micrograph of a Γ_{6k} bundled actin sample. Scale bar = 50 μm. (b) FRET fluorescence lifetime overlay of micrograph shown in (a). Color bar represents the distribution in fluorescence lifetimes measured in the sample. The black solid line represents the mean of the distribution. (c) Quartile box plots and confidence diamonds for mean donor–acceptor distance giving the mean intra-bundle spacing for Γ_{6k} and Γ_{20k}; NS denotes that the two distributions are statistically equivalent. For interpreting the box plots, the top and bottom of each box give the upper and lower quartiles where the box height represents 50% of the distribution. The horizontal line inside the box indicates the median value of the distribution. The top and bottom of the diamond are a 95% confidence interval for the mean. The middle of the diamond is the sample average, which is an estimate of the population mean.

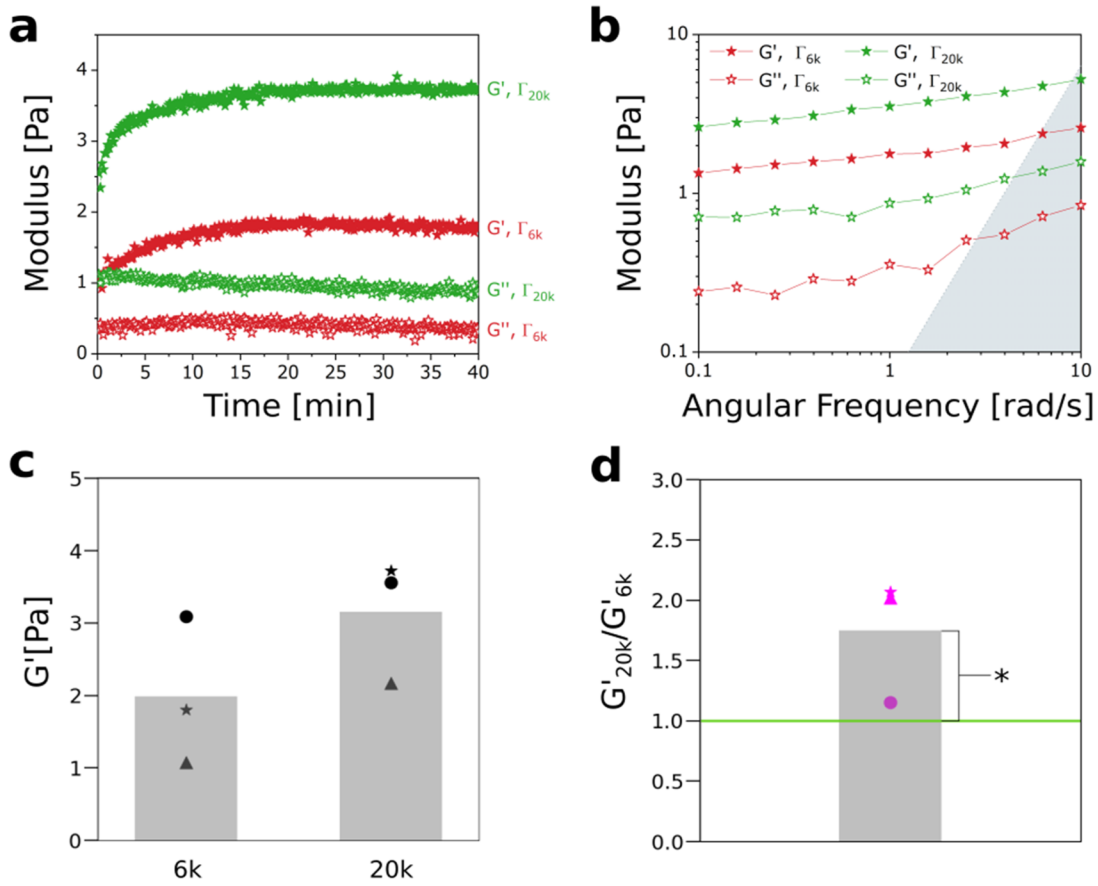

FIG. 5. (a) Time sweeps showing the evolution of the storage moduli, G' (closed stars), and loss moduli, G'' (open stars), of the bundled actin networks formulated with Γ_{6k} (red) and Γ_{20k} (green). (b) Frequency sweeps performed at 2% strain measured G' (closed stars) and G'' (open stars) of the bundled actin networks formulated with Γ_{6k} (red) and Γ_{20k} (green). The shaded region indicates conditions under which inertia is expected to dominate the measured torque. (c) Bar graphs for conical geometry measurements, with each replicate represented by a different shape. These distributions are not statistically significantly different from one another. (d) Bar graph of normalized storage moduli for all replicates for the conical geometry data. Distinct replicates are shown using shapes, with conical geometry shapes matching panel (c). Z-score comparison assuming that data are normally distributed gives a significant difference between G'_{20k}/G'_{6k} and unity (G'_{6k}/G'_{6k}), indicated by the green line, with a p-value of 0.04 (*) for the conical geometry and <0.000 01 (****) for the parallel plate geometry.

networks can be affected by the magnitude of the applied strain, differences in the moduli of networks formed at 1% and 2% are within error,[53] and thus, the effect of the applied strain during gelation is not considered significant here. The networks were also characterized through frequency sweeps. Figure 5(b) shows the frequency sweeps performed on the same replicate as in Fig. 5(a). G' and G'' both exhibit a frequency-dependent behavior, and at all frequencies, $G' > G''$. In addition, strain sweeps on the formed networks can be seen in Fig. S7. Figure 5(c) shows G' from the plateau in the time sweeps for all CG replicates. A representative evolution of G' for PPG is shown in the supplementary material (Fig. S8). Notably, across all replicates, G' is higher for Γ_{20k} than for Γ_{6k}, suggesting that a stiffer network is formed when a higher molecular weight PEG chain is used. When comparing PPG and CG distributions in G', we observe that they are statistically different via t-test with p-values of 0.05 and 0.03 for Γ_{6k} and Γ_{20k}, respectively. This difference is attributed to the onset of inertial effects for the PPG, indicated by a phase angle greater than 170°.[54] In Fig. 5(d), we normalize within each CG replicate to the long-time steady-state value of Γ_{6k}. This normalization procedure eliminates the systematic variation associated with the pipetting variance between replicates. With this analysis, we find that Γ_{20k} G' replicates are stiffer than Γ_{6k} replicates. We note that at PEG concentrations on the order of those examined here, solutions of 6k and 20k PEG both have viscosities of about 1 mPa s.[55] Thus, the differences in the rheological properties of Γ_{6k} and Γ_{20k} cannot be attributed to differences in the rheological properties of the polymer solutions and are instead attributed to weak vs strong bundling in the networks.

DISCUSSION

Fixed-mass depletion in relation to living cells

We sought to understand how the strength of depletion interactions varies when the total depletant mass is held fixed, a.k.a. fixed-mass depletion. By framing this inquiry in the context of the Asakura–Oosawa model, we are able to show that the interaction potential scales as q^{ζ}. For the fixed volume fraction case, we report values of $\zeta = -1$ for spheres and non-parallel rods and $\zeta = -\frac{1}{2}$ for parallel rods, showing that smaller depletants therefore increase the depletion interaction strength. Meanwhile, for the fixed mass density case, we saw the sign of ζ flip such that $\zeta = \frac{1}{3}$ for spheres and non-parallel rods and $\zeta = \frac{1}{6}$ for parallel rods. Thus, when PEG depletant mass density is held fixed, the depletion interaction strength increases, rather than decreases.

Our simulations are qualitatively consistent with the scaling prediction for fixed mass density, although differences between the two make a direct quantitative comparison difficult for a few reasons. First, the range of q between the scaling model and simulation does not overlap. The AO model is exact for $q < 0.1547$.[30] While only exact in this range, previous studies have shown it to be a viable approximation for larger values of q.[31,32] In our simulations, we explore depletant that extends beyond this threshold (cf. Fig. 1). However, we still observe the same expected trend given by the scaling arguments—interaction strength increases as we increase the PEG molecular weight. Second, we do not have a reliable quantitative measure of $U^*(q)$ in simulation, although the presence of thicker bundles and larger mesh sizes are indications of stronger depletion interactions (cf. Fig. 1). Thus, although we cannot experimentally access the exact magnitude of ζ in simulation, we can determine its sign to be positive. Third, our analytical model does not account for the semiflexible nature of the polymers. Despite this, we suspect that the key result pertaining to fixed mass-density depletion could extend to a broader class of semiflexible polymers as evidenced by the results of our simulation—which do consider actin filaments as semiflexible polymers. Fourth, simulations include Lennard-Jones interactions, which are absent from the Asakura–Oosawa model as well as in our scaling argument. Quantifying how these effects contribute to the interaction potential in the context of fixed-mass depletion would be an interesting area of further study.

We corroborate our predictions from simulation via experiment—capturing a morphological difference between the weakly bundled and strongly bundled states by systematically varying the PEG molecular weight and concentration. We observe that the morphology of the network becomes increasingly bundled along both axes (cf. Fig. 2). However, we find one difference between simulation and experiment, namely the nature of how the system varies across single filament, weakly bundled, and strongly bundled regimes. In the model, we observe a more gradual change, whereas in experiment, the change from one morphology to the next is much more distinct. One plausible cause is finite size effects; while the simulation study consists of 200 actin filaments, the experiments study systems have $O(10^3)$ actin filaments. Furthermore, for computational simplicity, the actin filaments in the simulations were assumed to be about an order of magnitude shorter than in experiments. This effectively reduced the separation between the actin and PEG length-scales in the simulations compared to the experiments, potentially making the morphological changes in simulations less sharp, as compared to the experiments. The model configuration space is built from a choice of model specific interaction parameters (see Methods). These parameters were tuned to recover the same qualitative morphological behavior as observed in experiment. In future work, these parameters could be systematically tuned to investigate the effects of changing model interaction strengths, which would likely recover the more abrupt morphological difference observed experimentally.

An important consideration is that PEG is not a protein. As shown before, for PEG, $R_g \sim MW^{\nu}$ with $\nu = \frac{3}{5}$. For proteins, the radius of gyration has been modeled as being proportional to $MW^{1/3}$,[27] which, for the analytical case of two spheres, gives a scaling equivalent to that of a spherical colloid, $\zeta = -\frac{1}{2}$ as before. Fitting experimental data for a combination of different proteins,[56] as well as other experimental work,[57] gives a scaling of $R_g \sim MW^{2/5}$. This exponent $\nu = \frac{2}{5}$ gives a U^* that scales with q as $q^{-1/2}$ just as with spherical colloids. We note that the value of ν for which ζ becomes positive is $\nu = \frac{1}{2}$. Proteins, with their scaling exponent at $\nu = \frac{2}{5}$, are just below this threshold. Despite not recovering the sign change we saw analytically for the case of proteins, we believe that further exploration of fixed-mass depletion is of interest in a cellular context.[3,10] It is clear that the Asakura–Oosawa model does not provide a complete description. For instance, the ATP-dependent activity in the cell can enhance diffusion.[58] Furthermore, one could include electrostatic and van der Waals interactions. Finally, the Asakura–Oosawa model treats depletants as an ideal gas, an assumption that is only valid in the limit of low depletant concentrations. We note that the PEG concentrations in our study are more dilute than in cellular contexts. As such, we believe that the effect could be much stronger in cells due to macromolecular crowding.[27,59] We further note that the diameter of a typical crowding protein is ~5 nm, but the range of sizes varies within the cytosolic context.[3,60] The effect of depletant size polydispersity could additionally be taken into consideration. Future studies can focus on incorporating these effects to refine the form of U^* and determine if positive scaling is present within the cellular context when considering fixed-mass depletion. Furthermore, it would be interesting to determine if the magnitude and sign of ζ could be actively controlled to assist in dynamic intracellular organization.

Fixed-mass depletion in relation to material properties

Confocal microscopy indicated that to the left of the blue line [cf. Fig. 2(a)], actin filaments coexist with bundles. To the right of this line, the entire network appears to be incorporated into bundles. The difference in our test configurations, Γ_{6k} and Γ_{20k} states, is supported by DLS analysis (cf. Fig. 3). The fitted relaxation times for each condition are significantly different and match our observations in confocal microscopy. Namely, as the molecular weight of the PEG polymers increases, the relaxation time increases because a greater fraction of the network is bundled. The stretched exponent also decreases, indicating a greater heterogeneity in the distribution of bundle sizes. The Γ_{20k} condition, by nature of being forced into the bundled regime, is most likely to be kinetically arrested.[61] What

would have been free diffusion is limited by inter-bundle steric interactions. In contrast, the control condition (no PEG) is most freely diffusing; τ_f is small and the intensity pattern decorrelates quickly. Since the Γ_{6k} morphology exists as a mixture of the control condition and the Γ_{20k} condition, it combines the features of both the kinetic arrest and the free diffusion modes. Given this, one would expect that the stretched exponent would be smaller for the Γ_{6k} condition. However, the opposite is observed—where the stretched exponent is smallest for the Γ_{20k} condition. The reasoning for this is not clear within the context of this analysis. Further quantitative work with our scattering data is difficult when using Mie scattering assumptions, such as spherical particle shapes, which cannot be applied to actin filaments. Studies have shown that dynamic light scattering data can also be analyzed by changing the dynamic structure factor of the fit to a model suited for semiflexible polymers.[62–64] The decay rate associated with this semiflexible polymer dynamic structure factor depends on the persistence length of the polymer, which can be used as a fit parameter. With this type of analysis, we report values for the persistence lengths of the Γ_{6k} condition to the Γ_{20k} condition, which are statistically indistinguishable from each other, yet show increases in respective mean values (Fig. S9).

Previous work has characterized bundle size properties, such as the diameter.[28] The FRET analysis we presented here provides an additional measure on bundle geometry, namely the intra-bundle spacing between actin filaments. With PEG as a bundling agent, we expect the filament bundles to be in the fully coupled regime.[65] Our analysis gives us a measure on the distance associated with fully coupled actin filaments bundled by depletion forces. This could be extended to measure intra-bundle distance for different actin bundling proteins. Scaling out, the physics that limits the extent of bundle diameter is still very much an open question. When well-mixed, we observe that actin filaments bundle in a polydisperse way (Fig. S10), with bundles forming simultaneously across the full spatial extent of the system. Given this, there are two different mechanisms to consider. The first is the mechanism by which a free actin filament gets incorporated into a neighboring bundle. The other is the interaction between two mature bundles. For the formation of a single bundle, theoretical arguments have been proposed in terms of chirality,[66] packing defects,[67] and counterion repulsion.[68] Per the bundle–bundle interaction, arguments have been presented pointing to the interplay between surface–surface interactions and macroscopic hydrodynamic forces in the system.[24] The gels in our study exhibit the polydisperse incorporation of filaments into bundles across the full spatial extent of the system, both in the model and experimentally. The polydisperse morphology of bundles seen in the model only includes surface–surface interactions, suggesting that the hydrodynamic forces are not as dominant in determining subsequent network morphology. Future work could investigate the limitations on bundle diameter more systematically via similar measurement techniques to those presented in the main text and the supplementary material. On the scale of an individual bundle, electron microscopy and FRET measurements give bounds on the number of actin filaments incorporated into a bundle for states, and furthermore, these modalities inform that bundle diameter and intra-bundle spacing are equivalent across these morphological regimes (see the supplementary material). FRET also gives insights into the notion of effective cross-linking by parameterizing how close filaments within a bundle are to one another. Despite measuring the same intra-bundle spacing across our PEG samples, we note that we observe qualitative differences in the structure of fluorescence lifetime distributions (Fig. S12). One might expect to uncover physical signatures between different mechanisms that drive bundling based on extending the FRET methods outlined herein. We note that further characterization of similar gels has been performed, studying the water dynamics using 2DIR spectroscopy.[69]

When looking at the bulk properties of the gel, the storage modulus for Γ_{20k} is larger than for Γ_{6k} across all replicates, indicating a difference in gel stiffness. The Γ_{20k} condition has a longer diffusion lifetime as shown by dynamic light scattering measurements, perhaps due to the increased stiffness of the bulk material. We also note that we observe stronger gels than previously reported.[28] We suspect that this is due in part to the omission of gelsolin in the current work, which is known to truncate the length of actin filaments and could impact bulk network properties as a result. Furthermore, the current study uses 50 mM KCl vs 1M KCl. Using higher concentrations could impact filament–filament interactions and reduce gel stiffness. Control measurements indicate that the observed rheological differences are not due to changes in fluid viscosity due to the different PEG molecules (Fig. S13), or due to any shearing of the network while measuring with the rheometer during network formation (Fig. S14).

Previous work from Hosek and Tang[24] predicted that the critical concentration of bundling depends on PEG molecular weight and presented experimental results to validate their claim. In addition, our current study expands on this work by exploring the system below the critical concentration, namely the weakly bundled regimes to give a more complete characterization of the phase space for these networks. We note that studies examining the depletion of proteins by PEG have given similar agreement within the AO model when the proteins are modeled as hard spherocylinders and the PEG molecules are taken as ideal polymers.[70] Depletion of rods has been studied in other systems.[71–75] We observe similar morphologies in the work of Kazem *et al.*[75] where simulations giving network spanning bundle structure were observed as a result of underlying irregularity in the attraction of the rods. We suspect that the semiflexible nature of F-actin filaments and the filament-length polydispersity relate to this irregularity and result in network spanning bundle structure in our assay. In other rod depletion systems, the phase spaces resulting are quite different from the observed behavior in our study.[73] We attribute this to the fact that we are working in more dilute samples, which may give a simpler phase behavior. The scaling laws presented here focus on the pair potential minimum. Still, the integrated effect of the attractions is typically what determines the phase behavior. If the minimum of the fixed-mass depletion pair potential gets deeper with depletant molecular weight, then its second virial coefficient[76–78] will also become more negative (i.e., stronger integrated attractions) since its range grows. The fixed number density pair-potential minimum gets shallower with increasing molecular weight, but its range gets larger. It is not clear whether the second virial will become positive or negative. However, what is clear is that the integrated attractions of the fixed-mass case will become increasingly stronger than the fixed-number-density case as the molecular weight grows. This is an

important distinction since both the minimum and the range matter for thermodynamics. In this work, we have not sought to extend our analysis of fixed-mass depletion to the expected phase behavior. We have only started to get at this experimentally [cf. Fig. 2(a)]. This would be a potential avenue for future work.

CONCLUSION

In this study, we explored how the strength of depletion interaction potential U^* varies when the total depletant mass is held fixed, a.k.a. fixed-mass depletion. We answered this question by studying networks of reconstituted semiflexible actin *in silico* and *in vitro*. Our work gives insights into the biologically relevant phenomena of fixed-mass depletion and provides a more complete characterization of the depletion interaction, which is necessary to better understand the intracellular organization of the cytoskeleton.[3] We have demonstrated that actin morphology can be changed in a fixed-mass context, by changing the molecular weight of the PEG molecules that act as depletants in the system. The ability to dynamically change actin morphology via steric interactions in a crowded but dynamic environment is reminiscent of known mechanisms in living cells, such as within condensates[79] or macromolecular crowding.[59] Future work could explore other areas of our configuration space using similar characterization techniques as done in this work.

Our work also provides a foundation for deriving semiflexible-polymer-based biomimetic materials that might embody some of life's dynamic ability for accomplishing mechanical tasks. Our identification of a morphological change from a weakly bundled state to a strongly bundled state offers insights to explain the dynamic properties of cell-based actin manipulation and perhaps a pathway toward harnessing this protein in artificial contexts. We have demonstrated control over actin network morphology and mechanics by steric interactions alone under the constraint of fixed mass of the depletants. A better mechanistic understanding of fixed-mass depletion could allow for *in situ* control over material properties by varying the size distribution of a closed system with fixed depletant mass (e.g., aggregation or lysis of depletants). Future work could leverage a similar numerical modeling framework to test for reversibility[24] in network morphology to help motivate studies into reversible soft matter materials.[80] Further developing this type of control could lead to novel strategies in developing bio-inspired materials that mimic cells' ability to dynamically mechanically adapt and respond to stimuli.[24,80]

METHODS

Actin preparation

Actin was purified from rabbit psoas skeletal muscle from Pel-Freez using a GE Superdex 200 Increase HiScale 16/40 column and stored at −80 °C in G-Buffer (2 mM tris-hydrochloride pH 8.0, 0.2 mM disodium adenosine triphosphate (ATP), 0.2 mM calcium chloride, and 0.2 mM dithiothreitol). All protein stocks were clarified of aggregated proteins at 100 000 g for 5 min upon thawing and used within 7 days. The G-actin concentration in the supernatant was determined by measuring the solution absorbance at 290 nm with a NanoDrop 2000 (Thermo Scientific, Wilmington, DE, USA) and using an extinction coefficient of 26 600 M^{-1} cm^{-1}.

Confocal microscopy

Samples were prepared to yield a final buffer concentration of 20 mM imidazole pH 7.4, 50 mM potassium chloride (KCl), 2 mM magnesium chloride ($MgCl_2$), 1 mM dithiothreitol, 0.1 mM ATP, 1 mM trolox, 2 mM protocatechuic acid (PCA), and 0.1 mM protocatechuic 3,4-dioxygenase (PCD). The polyethylene glycol, KCl, imidazole, dithiothreitol, and $MgCl_2$ were purchased from Sigma-Aldrich. The adenosine triphosphate and trolox were purchased from Fisher Scientific. PCA was purchased from the HWI Group. PCD was purchased from Sigma-Aldrich.

Glass flow cells were prepared by sonication of individual slides in water for 5 min, followed by blow-drying with nitrogen. These slides were then placed in a base piranha solution of five parts DI water, one part 30% hydrogen peroxide, and one part 30% ammonium hydroxide for 30 min at 80 °C. These slides were then sonicated again for 5 min, blow-dried with nitrogen, and stored in isopropanol until use. Thick coverslips and thin slides were attached by means of melting Parafilm with pre-cut chambers, which are then treated with potassium hydroxide for 10 min to activate hydroxyl groups on the glass surface and then passivated with 0.2 mg/ml poly-l-lysine-g-polyethylene-glycol from Nanosoft Polymers in a humid environment.[81]

We used an Olympus FV1000 motorized inverted IX81 microscope suite, with instrument computer running FV10-ASW software version 4.2b, to image actin networks using laser-scanning confocal microscopy. Actin filaments were labeled with rhodamine–phalloidin on a one-to-one molar ratio and excited with 543 nm wavelength laser light. Each sample of actin was prepared once and imaged in three random, well-separated locations.

Each z-stack taken was processed using ImageJ. The image was opened, and a maximum z-projection across 25.5 μm through the bulk of the image was produced. The laser intensity was kept constant across all experiments to determine the presence or absence of a filamentous background network of actin between bundles. Strongly bundled samples included a small fraction (up to ≈0.15%) of saturated pixels. For each confocal z-stack, both the degree of bundling and the mesh size were algorithmically determined (see the supplementary material).

Rheology

Experiments were performed on a TA Discovery HR 20 rheometer fitted with either a 20 mm, 2° stainless steel cone geometry or an 8 mm parallel plate. Master buffer was prepared according to the steps described in the Confocal microscopy section, else the PCA, PCD, and trolox. Master buffer was mixed by pipette with deionized water and PEG molecules of appropriate molecular weight and in the desired concentration. Actin was then added and mixed gently by pipette before adding to a 1:1M ratio, actin:phalloidin. After combining and mixing with dried phalloidin, the sample was pipetted onto the rheometer with a total volume of 75 μl. Throughout all experiments, a temperature-controlled Peltier plate maintained the temperature at 25 °C, and a solvent trap was utilized to prevent evaporation during data acquisition. Immediately after loading the sample, a time sweep was started to monitor the evolution of the shear moduli over time. The time sweeps were performed at 2% strain and a frequency of 1 rad/s. These parameters were selected

based on strain sweeps performed at 1 rad/s (Fig. S7) and frequency sweeps performed at 2% strain.

Dynamic light scattering

Actin and master buffer were prepared according to the steps described in the Confocal microscopy section, else the PCA, PCD, and trolox. Phalloidin in methanol was dried using compressed nitrogen gas and added to the sample solution in a 1:1M ratio with the actin to stabilize the filaments and prevent depolymerization. 45 μl was imaged in a Malvern Zetasizer Nano ZS instrument for five runs for each sample. The refractive index of the master buffer was found to be 1.334, and the refractive index of actin was found to be 1.3343.

Particles in a fluid are known to scatter incident light. The diffusion of the suspended particles changes the reported intensity at each angle measured; therefore, using a directed laser, it is possible to use the intensity measurement across multiple temporal decades to understand the Brownian dynamics of the particles in solution. This is done by measuring the diffraction field at a given time τ and then re-measuring the sample at some later time,[82]

$$G_2(\tau) - 1 = G_1(\tau) = \sigma^2\left(e^{-\left(\frac{\tau}{\tau_f}\right)^{\beta}}\right)^2. \tag{8}$$

For spherical particles, this is usually accomplished using the Stokes–Einstein equation, which directly gives the hydrodynamics radius. However, for non-spherical particles, this calculation is no longer valid, and a quantitative comparison requires a calculation of the stretched exponent β.

FRET

G-actin, Atto 488, and Alexa Fluor 555 maleimide dye (Thermo Fisher) were thawed, 1 ml G-buffer 1× was prepared, and protein stock was clarified of aggregates as described above. The volume of dye needed to achieve an excess of 10× dye to protein was calculated. The dye was added to G-actin solution and mixed thoroughly by pipette prior to 2 h of incubation at room temperature, allowing the dye to bind actin cysteines. During incubation, Princeton 20 Centri-Spin columns are hydrated with 650 μl of G-buffer, allowing the resin to swell for 30 min. After incubation, the hydrated columns were placed in a centrifuge and spun at 700 g for 2 min to remove excess G-buffer. The dyed protein solution was then added to the hydrated column by pipette, being careful to avoid the edges of the column while pipetting. The columns were then placed in a centrifuge and spun at 700 g for 2 min, where the gel filtration column effectively separates the actin from the free dye. Concentrations were then measured via NanoDrop. Labeled G-actin was aliquoted, flash-frozen with liquid nitrogen, and stored at −80 °C until experimentation.

Sample chambers are constructed with piranha etched no. 1.5 glass microscope coverslips and 2 mm thick silicon gaskets with a 5 mm diameter hole punched out. Prior to assembly, the slides and gaskets are treated in a Hellmanex solution at 80 °C for 20 min to ensure adhesion between the two components. 30 min prior to addition of protein samples, the chambers are passivated with 1 mg/ml bovine serum albumin (BSA)—purchased from Sigma-Aldrich—to prevent interactions between the actin and the glass slide. During slide passivation, the sample is mixed via a multi-step procedure. The first step is preparing donor seed filaments where half of the total sample, deionized water, and master buffer are mixed with the volume of donor-labeled (Atto 488) actin monomers by pipette. This polymerizes the donor filaments, which are then stabilized by adding to 1:1 phalloidin. The donor seed filaments are then added to the other half of the total sample, deionized water, and master buffer along with PEG molecules, acceptor-labeled (Alexa Fluor 555) actin, and unlabeled actin monomers and mixed gently by pipette. This is then added to 1:1 phalloidin to stabilize the filaments. The BSA in the sample well is removed by washing five times with master buffer. After the final wash, the master buffer is removed and 20 μl of combined protein sample is added to the sample well. The final concentration for all samples is as follows: [Atto 488 actin] = 0.1 μM, [Alexa Fluor 555 actin] = 1.0 μM, and [total actin] = 12 μM.

The sample was loaded onto a home-built time-correlated single photon counting (TCSPC) confocal fluorescence microscope. The microscope utilizes a 486 nm picosecond laser with a 50 MHz repetition rate and laser power set to 50 μW via neutral density attenuation. For all samples, the laser focus was placed at a depth of 5 μm from the base of the microscope slide using a Mad City Laboratories piezo stage and translated via micrometer adjustment in the x and y dimensions to navigate to different spatial locations. Emitted photons were collected using a 1.45 NA, 100× magnification microscope objective and routed through a pinhole and 511/10 bandpass emission filter toward a Hamamatsu GaAsP photomultiplier tube. Photomultiplier output pulses were then amplified and counted with a Becker and Hickl (BH) TCSPC computer card. For each replicate, three random, well-separated regions were imaged to incorporate intra-sample variation in our results.

Lifetime data were analyzed using the BH SPCImage software where decay-matrix calculations were performed to generate a distribution of fluorescence lifetimes within an image. The quantity τ_{DA} is determined from this distribution in fluorescence lifetimes. The quantity τ_D was determined with a control study where the distribution of fluorescence lifetimes was measured for actin filaments that were only labeled with the donor. The average donor-to-acceptor distance was then calculated using Eqs. (1) and (2).

Simulation parameters

The actin bead-chains have a uniform length of 160 nm and a bead diameter σ of 8 nm, and the diameter of the PEG spheres is varied from 0.25 σ to 0.75 σ. All distances in the simulations are scaled by σ, and all times are scaled by τ = 0.1 s.[83] All energies in the model system are scaled by kT. The simulation box size is set to 75 σ by 75 σ by 10 σ across all simulations, and periodic boundary conditions are enforced.

To understand how the (1) concentration and (2) molecular weight of the PEG particles influenced the actin bundling, we vary (1) the number of PEG particles from 4000 to 10 000 while keeping the simulation box volume unchanged and (2) PEG particle radius from 2 to 6 nm. To convert from PEG radius of gyration (R_g) to molecular weight (MW), we assumed the classic result from Flory theory, $R_g \propto MW^{3/5}$. This gives molecular weights of 6k, 20k, and

37.4k for radii of 0.25 σ, 0.5 σ, and 0.75 σ respectively. The PEG concentration is varied from 4000 $\frac{V_\rho}{V_{box}}$, 5000 $\frac{V_\rho}{V_{box}}$, 6000 $\frac{V_\rho}{V_{box}}$, and 10 000 $\frac{V_\rho}{V_{box}}$, where $V_\rho = \frac{4}{3}\pi r^3$, with r representing the effective radius of the PEG particle, and V_{box} is the volume of the simulation box, which is 56 250 σ^3. We explore 12 different systems to determine the effects of PEG concentration and effective molecular weight. The number of actin filaments is held constant at 200 for all 12 systems.

For the Lennard-Jones pairwise interactions, $\varepsilon_{\text{PEG–PEG}}$ is set to 1.25 for attractive interactions and 1.0 for repulsive interactions and $\varepsilon_{\text{actin–actin}}$ is set to 0.3 for attractive interactions and 1.0 for repulsive interactions. We encode only repulsive interactions between the PEG beads and the actin strands, and $\varepsilon_{\text{PEG–actin}}$ is equal to 2.0.

SUPPLEMENTARY MATERIAL

The supplementary material contains additional material and analysis from this study and is divided into sections. The Mesh size determining algorithm section (Fig. S1) contains a description of the algorithm used to determine the mesh size in this study. The PEG clustering section (Fig. S2) contains additional data related to PEG clustering during simulations. The Number density view of confocal data section (Fig. S3) contains the data from Fig. 2(a) recast into a number density x-axis. The Degree of bundling algorithm section (Fig. S4) contains a description of how the degree of bundling was determined for the confocal micrographs in this study. The Actin filament length distribution section gives results for the distribution in lengths for F-actin in this work (Fig. S5). The Dynamic light scattering section (Fig. S6) contains raw DLS curves corresponding to the results shown in Fig. 3. The Rheology section (Figs. S7 and S8) contains additional rheology data obtained in this study including strain sweeps and parallel plate geometry data. The Estimation of persistence length section (Fig. S9) provides an estimation of the persistence length of actin bundles based on an alternative fit equation used on the DLS data. The Electron microscopy section (Fig. S10) provides additional methods and characterization data of the Γ_{6k} and Γ_{20k} states using electron microscopy. The section on Bounds for number of filaments in a bundle combines analysis from FRET and electron microscopy to give bounds on the number of filaments in a bundle. The Contact potential as a function of depletant size section (Fig. S11) provides a plot of the scaled AO interaction potential with respect to varying depletant sizes. The section on FRET control measurements contains additional FRET data, including control measurements (Fig. S12). The section on Examining viscosity effects on rheology contains a control experiment testing the viscosity of our PEG solutions (Fig. S13). The section on Examining shear effects on rheology results contains a control experiment testing for the effect of applied shear during gelation on rheology results (Fig. S14). The section on Additional confocal microscopy representations contains additional representations of the confocal microscopy imaging results obtained in this study (Fig. S15).

ACKNOWLEDGMENTS

This research was primarily supported by the National Science Foundation through the Center for Dynamics and Control of Materials: an NSF MRSEC under Cooperative Agreement Nos. DMR-1720595 and DMR-2308817 with additional support from the Welch Foundation (Grant Nos. F-1848 and F-1696) and Grant No. NSF DMR-2144380. The authors acknowledge the use of facilities and instrumentation supported by the National Science Foundation through the Center for Dynamics and Control of Materials: an NSF MRSEC under Cooperative Agreement No. DMR-1720595. We also acknowledge the Texas Materials Institute for the use of facilities and instrumentation. We recognize Carlos Baiz and Xiaobing Chen for insightful discussions. We also acknowledge Vernita Gordon for use of her confocal microscope, as well as Raluca Gearba-Dolocan for assistance with electron microscopy. José Alvarado and Moumita Das acknowledge the Isaac Newton Institute for Mathematical Sciences, Cambridge, for support and hospitality during the program—New statistical physics in living matter: non equilibrium states under adaptive control—where work on this paper was undertaken. This work was supported by EPSRC Grant No. EP/K032208/1. Additionally, L.M. and M.D. acknowledge partial support from DMR-2118449.

AUTHOR DECLARATIONS

Conflict of Interest

The authors have no conflicts to disclose.

Author Contributions

James Clarke is the main contributor of this work. Lauren Melcher, Anne Crowell, and Francis Cavanna are recognized as having contributed equally to this work. Lauren Melcher led the development and analysis of the simulation and its results with Moumita Das. Anne Crowell helped perform all rheological experiments and wrote much of the analysis and methods related to rheology. Francis Cavanna performed the preparation and confocal imaging of actin networks, as well as the preparation for DLS imaging. Justin Houser helped prototype FRET experiments and provided direct assistance in all FRET data acquisition. Allison Green performed the DLS measurements, fitted the stretched exponential and relaxation time parameters, and provided insights and analysis with Delia Milliron. Kristin Graham helped with acceptor–donor labeling for actin-FRET measurements, along with experimental planning for all FRET data acquisition. Tom Truskett provided insights into the nature of morphological differences, as well as limitations on bundle diameter. Adrianne Rosales was instrumental in conceptually designing rheological experiments and provided consistent feedback and insights as the experiments progressed. Jeanne Stachowiak was instrumental in planning FRET experiments. Moumita Das helped to develop the model and assisted in the interpretation of the simulation results; Moumita Das and Jose Alvarado developed the scaling analyses of the model. José Alvarado planned most of the inter-lab experimentation, assisted in the interpretation of all the results, and provided direct feedback on the structure and material of this paper.

James Clarke: Data curation (equal); Formal analysis (equal); Investigation (equal); Methodology (equal); Project administration (equal); Software (equal); Validation (equal); Writing – original draft (equal); Writing – review & editing (equal). **Lauren Melcher**: Data curation (supporting); Formal analysis (supporting); Software

(equal); Writing – original draft (supporting); Writing – review & editing (supporting). **Anne D. Crowell**: Formal analysis (supporting); Investigation (supporting); Methodology (supporting); Writing – original draft (supporting); Writing – review & editing (supporting). **Francis Cavanna**: Formal analysis (supporting); Investigation (supporting); Methodology (supporting); Writing – original draft (supporting); Writing – review & editing (supporting). **Justin R. Houser**: Methodology (supporting); Supervision (supporting); Writing – review & editing (supporting). **Kristin Graham**: Methodology (supporting); Resources (supporting); Writing – review & editing (supporting). **Allison M. Green**: Investigation (supporting); Methodology (supporting); Writing – review & editing (supporting). **Jeanne C. Stachowiak**: Conceptualization (equal); Funding acquisition (equal); Writing – review & editing (supporting). **Thomas M. Truskett**: Conceptualization (equal); Funding acquisition (equal); Writing – review & editing (supporting). **Delia J. Milliron**: Conceptualization (equal); Funding acquisition (equal); Writing – review & editing (supporting). **Adrianne M. Rosales**: Conceptualization (equal); Funding acquisition (equal); Resources (supporting); Writing – review & editing (supporting). **Moumita Das**: Conceptualization (equal); Funding acquisition (equal); Writing – original draft (supporting); Writing – review & editing (supporting). **José Alvarado**: Conceptualization (equal); Funding acquisition (equal); Writing – original draft (equal); Writing – review & editing (equal).

DATA AVAILABILITY

The data that support the findings of this study are available from the corresponding author upon reasonable request.

REFERENCES

[1] J. Alvarado, B. M. Mulder, and G. H. Koenderink, "Alignment of nematic and bundled semiflexible polymers in cell-sized confinement," Soft Matter **10**, 2354–2364 (2014).

[2] H. N. W. Lekkerkerker and R. Tuinier, *Colloids and the Depletion Interaction* (Springer, Dordrecht, 2011).

[3] D. Marenduzzo, K. Finan, and P. R. Cook, "The depletion attraction: An underappreciated force driving cellular organization," J. Cell Biol. **175**, 681–686 (2006).

[4] H. N. W. Lekkerkerker and R. Tuinier, "Phase transitions of hard spheres plus colloids," in *Colloids and the Depletion Interaction*, edited by H. N. W. Lekkerkerker and R. Tuinier (Springer, Dordrecht, Netherlands, 2011), pp. 177–195.

[5] A. M. Green *et al.*, "Depletion-driven assembly of polymer-coated nanocrystals," J. Phys. Chem. C **126**, 19507–19518 (2022).

[6] T. Schilling, S. Jungblut, and M. A. Miller, "Depletion-induced percolation in networks of nanorods," Phys. Rev. Lett. **98**, 108303 (2007).

[7] G. H. Lai *et al.*, "Self-organized gels in DNA/F-actin mixtures without crosslinkers: Networks of induced nematic domains with tunable density," Phys. Rev. Lett. **101**, 218303 (2008).

[8] C. Zhang, P. G. Shao, J. A. van Kan, and J. R. C. van der Maarel, "Macromolecular crowding induced elongation and compaction of single DNA molecules confined in a nanochannel," Proc. Natl. Acad. Sci. U. S. A. **106**, 16651–16656 (2009).

[9] T. Sanchez, D. T. N. Chen, S. J. DeCamp, M. Heymann, and Z. Dogic, "Spontaneous motion in hierarchically assembled active matter," Nature **491**, 431–434 (2012).

[10] G. E. Neurohr and A. Amon, "Relevance and regulation of cell density," Trends Cell Biol. **30**, 213–225 (2020).

[11] E. S. Chhabra and H. N. Higgs, "The many faces of actin: Matching assembly factors with cellular structures," Nat. Cell Biol. **9**, 1110–1121 (2007).

[12] R. Dominguez and K. C. Holmes, "Actin structure and function," Annu. Rev. Biophys. **40**, 169–186 (2011).

[13] S. Tojkander, G. Gateva, and P. Lappalainen, "Actin stress fibers—Assembly, dynamics and biological roles," J. Cell Sci. **125**, 1855–1864 (2012).

[14] J. R. Bartles, L. Zheng, A. Li, A. Wierda, and B. Chen, "Small espin: A third actin-bundling protein and potential forked protein ortholog in brush border microvilli," J. Cell Biol. **143**, 107–119 (1998).

[15] N. Castaneda *et al.*, "Cations modulate actin bundle mechanics, assembly dynamics, and structure," J. Phys. Chem. B **122**, 3826–3835 (2018).

[16] T. E. Angelini, H. Liang, W. Wriggers, and G. C. L. Wong, "Like-charge attraction between polyelectrolytes induced by counterion charge density waves," Proc. Natl. Acad. Sci. U. S. A. **100**, 8634–8637 (2003).

[17] J. X. Tang, T. Ito, T. Tao, P. Traub, and P. A. Janmey, "Opposite effects of electrostatics and steric exclusion on bundle formation by F-actin and other filamentous polyelectrolytes," Biochemistry **36**, 12600–12607 (1997).

[18] R. Uribe and D. Jay, "A review of actin binding proteins: New perspectives," Mol. Biol. Rep. **36**, 121–125 (2009).

[19] N. Elkhatib *et al.*, "Fascin plays a role in stress fiber organization and focal adhesion disassembly," Curr. Biol. **24**, 1492–1499 (2014).

[20] D. S. Courson and R. S. Rock, "Actin cross-link assembly and disassembly mechanics for α-actinin and fascin," J. Biol. Chem. **285**, 26350–26357 (2010).

[21] T. P. Stossel *et al.*, "Filamins as integrators of cell mechanics and signalling," Nat. Rev. Mol. Cell Biol. **2**, 138–145 (2001).

[22] K. M. Schmoller, O. Lieleg, and A. R. Bausch, "Structural and viscoelastic properties of actin/filamin networks: Cross-linked versus bundled networks," Biophys. J. **97**, 83–89 (2009).

[23] A. W. C. Lau, A. Prasad, and Z. Dogic, "Condensation of isolated semi-flexible filaments driven by depletion interactions," Europhys. Lett. **87**, 48006 (2009).

[24] M. Hosek and J. X. Tang, "Polymer-induced bundling of *F* actin and the depletion force," Phys. Rev. E **69**, 051907 (2004).

[25] S. Köhler, O. Lieleg, and A. R. Bausch, "Rheological characterization of the bundling transition in F-actin solutions induced by methylcellulose," PLoS One **3**, e2736 (2008).

[26] P.-G. de. Gennes, *Scaling Concepts in Polymer Physics* (Cornell University Press, 1979).

[27] A. P. Minton, "The influence of macromolecular crowding and macromolecular confinement on biochemical reactions in physiological media," J. Biol. Chem. **276**, 10577–10580 (2001).

[28] R. Tharmann, M. M. A. E. Claessens, and A. R. Bausch, "Micro- and macrorheological properties of actin networks effectively cross-linked by depletion forces," Biophys. J. **90**, 2622–2627 (2006).

[29] S. Asakura and F. Oosawa, "On interaction between two bodies immersed in a solution of macromolecules," J. Chem. Phys. **22**, 1255–1256 (1954).

[30] K. Binder, P. Virnau, and A. Statt, "Perspective: The Asakura Oosawa model: A colloid prototype for bulk and interfacial phase behavior," J. Chem. Phys. **141**, 140901 (2014).

[31] A. A. Louis, P. G. Bolhuis, E. J. Meijer, and J. P. Hansen, "Polymer induced depletion potentials in polymer-colloid mixtures," J. Chem. Phys. **117**, 1893–1907 (2002).

[32] A. A. Louis, R. Finken, and J.-P. Hansen, "The structure of colloid-polymer mixtures," Europhys. Lett. **46**, 741 (1999).

[33] S. Krüger, H.-J. Mögel, M. Wahab, and P. Schiller, "Depletion force between anisometric colloidal particles," Langmuir **27**, 646–650 (2011).

[34] F. Gittes, B. Mickey, J. Nettleton, and J. Howard, "Flexural rigidity of microtubules and actin filaments measured from thermal fluctuations in shape," J. Cell Biol. **120**, 923–934 (1993).

[35] A. Ott, M. Magnasco, A. Simon, and A. Libchaber, "Measurement of the persistence length of polymerized actin using fluorescence microscopy," Phys. Rev. E **48**, R1642–R1645 (1993).

[36] P. B. Moore, H. E. Huxley, and D. J. DeRosier, "Three-dimensional reconstruction of F-actin, thin filaments and decorated thin filaments," J. Mol. Biol. **50**, 279–292 (1970).

[37]J. A. Spudich, H. E. Huxley, and J. T. Finch, "Regulation of skeletal muscle contraction: II. Structural studies of the interaction of the tropomyosin-troponin complex with actin," J. Mol. Biol. **72**, 619–632 (1972).
[38]P. Nelson, *Biological Physics* (W. H. Freeman, 2003), Updated Edition.
[39]J. D. Weeks, D. Chandler, and H. C. Andersen, "Role of repulsive forces in determining the equilibrium structure of simple liquids," J. Chem. Phys. **54**, 5237–5247 (1971).
[40]F. Cavanna and J. Alvarado, "Quantification of the mesh structure of bundled actin filaments," Soft Matter **17**, 5034–5043 (2021).
[41]A. Fernandez-Nieves and A. M. Puertas, *Fluids, Colloids and Soft Materials: An Introduction to Soft Matter Physics* (John Wiley & Sons, 2016).
[42]M. Y. Tsang *et al.*, "Controlled sequential assembly of metal-organic polyhedra into colloidal gels with high chemical complexity," Small Struct. **3**, 2100197 (2022).
[43]Y. Tseng, K. M. An, and D. Wirtz, "Microheterogeneity controls the rate of gelation of actin filament networks," J. Biol. Chem. **277**, 18143–18150 (2002).
[44]J. Alvarado, L. Cipelletti, and G. H. Koenderink, "Uncovering the dynamic precursors to motor-driven contraction of active gels," Soft Matter **15**, 8552–8565 (2019).
[45]L. Wu *et al.*, "Förster resonance energy transfer (FRET)-based small-molecule sensors and imaging agents," Chem. Soc. Rev. **49**, 5110–5139 (2020).
[46]W. T. Snead *et al.*, "Membrane fission by protein crowding," Proc. Natl. Acad. Sci. U. S. A. **114**, E3258–E3267 (2017).
[47]J. R. Houser, C. C. Hayden, D. Thirumalai, and J. C. Stachowiak, "A Förster resonance energy transfer-based sensor of steric pressure on membrane surfaces," J. Am. Chem. Soc. **142**, 20796–20805 (2020).
[48]S. S. Vogel, B. W. van der Meer, and P. S. Blank, "Estimating the distance separating fluorescent protein FRET pairs," Methods **66**, 131–138 (2014).
[49]M. V. Sataric, D. L. Sekulic, and B. M. Sataric, "Actin filaments as the fast pathways for calcium ions involved in auditory processes," J. Biosci. **40**, 549–559 (2015).
[50]M. L. Gardel *et al.*, "Scaling of F-actin network rheology to probe single filament elasticity and dynamics," Phys. Rev. Lett. **93**, 188102 (2004).
[51]J. H. Shin, M. L. Gardel, L. Mahadevan, P. Matsudaira, and D. A. Weitz, "Relating microstructure to rheology of a bundled and cross-linked F-actin network *in vitro*," Proc. Natl. Acad. Sci. U. S. A. **101**, 9636–9641 (2004).
[52]J. X. Tang, P. A. Janmey, T. P. Stossel, and T. Ito, "Thiol oxidation of actin produces dimers that enhance the elasticity of the F-actin network," Biophys. J. **76**, 2208–2215 (1999).
[53]O. Esue, Y. Tseng, and D. Wirtz, "Mechanical shear can accelerate the gelation of actin filament networks," Phys. Rev. Lett. **95**, 048301 (2005).
[54]R. H. Ewoldt, M. T. Johnston, and L. M. Caretta, "Experimental challenges of shear rheology: How to avoid bad data," in *Complex Fluids in Biological Systems: Experiment, Theory, and Computation*, edited by S. E. Spagnolie (Springer, New York, 2015), pp. 207–241.
[55]S. Kirinčič and C. Klofutar, "Viscosity of aqueous solutions of poly(ethylene glycol)s at 298.15 K," Fluid Phase Equilib. **155**, 311–325 (1999).
[56]L. He and B. Niemeyer, "A novel correlation for protein diffusion coefficients based on molecular weight and radius of gyration," Biotechnol. Prog. **19**, 544–548 (2003).
[57]L. Hong and J. Lei, "Scaling law for the radius of gyration of proteins and its dependence on hydrophobicity," J. Polym. Sci., Part B: Polym. Phys. **47**, 207–214 (2009).
[58]S. C. Weber, A. J. Spakowitz, and J. A. Theriot, "Nonthermal ATP-dependent fluctuations contribute to the in vivo motion of chromosomal loci," Proc. Natl. Acad. Sci. U. S. A. **109**, 7338–7343 (2012).
[59]R. J. Ellis, "Macromolecular crowding: Obvious but underappreciated," Trends Biochem. Sci. **26**, 597–604 (2001).
[60]D. Marenduzzo, C. Micheletti, and P. R. Cook, "Entropy-driven genome organization," Biophys. J. **90**, 3712–3721 (2006).
[61]T. T. Falzone, M. Lenz, D. R. Kovar, and M. L. Gardel, "Assembly kinetics determine the architecture of α-actinin crosslinked F-actin networks," Nat. Commun. **3**, 861 (2012).
[62]E. Farge and A. C. Maggs, "Dynamic scattering from semiflexible polymers," Macromolecules **26**, 5041–5044 (1993).
[63]R. Götter, K. Kroy, E. Frey, M. Bärmann, and E. Sackmann, "Dynamic light scattering from semidilute actin solutions: A study of hydrodynamic screening, filament bending stiffness, and the effect of tropomyosin/troponin-binding," Macromolecules **29**, 30–36 (1996).
[64]K. Kroy and E. Frey, "Dynamic scattering from solutions of semiflexible polymers," Phys. Rev. E **55**, 3092–3101 (1997).
[65]M. M. A. E. Claessens, M. Bathe, E. Frey, and A. R. Bausch, "Actin-binding proteins sensitively mediate F-actin bundle stiffness," Nat. Mater. **5**, 748–753 (2006).
[66]G. M. Grason and R. F. Bruinsma, "Chirality and equilibrium biopolymer bundles," Phys. Rev. Lett. **99**, 098101 (2007).
[67]N. S. Gov, "Packing defects and the width of biopolymer bundles," Phys. Rev. E **78**, 011916 (2008).
[68]B.-Y. Ha and A. J. Liu, "Effect of non-pairwise-additive interactions on bundles of rodlike polyelectrolytes," Phys. Rev. Lett. **81**, 1011–1014 (1998).
[69]X. Chen, S. Roeters, F. Cavanna, J. Alvarado, and C. Baiz, "Crowding alters F-actin secondary structure and hydration," Commun. Biol. **6**, 900 (2023).
[70]R. Cheng *et al.*, "Protein–polymer mixtures in the colloid limit: Aggregation, sedimentation, and crystallization," J. Chem. Phys. **155**, 114901 (2021).
[71]B. Sung, H. H. Wensink, and E. Grelet, "Depletion-driven morphological transitions in hexagonal crystallites of virus rods," Soft Matter **15**, 9520–9527 (2019).
[72]Z. Dogic and S. Fraden, "Development of model colloidal liquid crystals and the kinetics of the isotropic–smectic transition," Philos. Trans. R. Soc., A **359**, 997–1015 (2001).
[73]M. Adams, Z. Dogic, S. L. Keller, and S. Fraden, "Entropically driven microphase transitions in mixtures of colloidal rods and spheres," Nature **393**, 349–352 (1998).
[74]Z. Dogic and S. Fraden, "Phase behavior of rod-like viruses and virus–sphere mixtures," in *Soft Matter* (John Wiley & Sons, Ltd., 2005), Vol. 1–86.
[75]N. Kazem, C. Majidi, and C. E. Maloney, "Gelation and mechanical response of patchy rods," Soft Matter **11**, 7877–7887 (2015).
[76]M. G. Noro and D. Frenkel, "Extended corresponding-states behavior for particles with variable range attractions," J. Chem. Phys. **113**, 2941–2944 (2000).
[77]R. J. Baxter, "Percus–Yevick equation for hard spheres with surface adhesion," J. Chem. Phys. **49**, 2770–2774 (1968).
[78]M. López de Haro *et al.*, "Virial coefficients and demixing in the Asakura–Oosawa model," J. Chem. Phys. **142**, 014902 (2015).
[79]Y. Shin and C. P. Brangwynne, "Liquid phase condensation in cell physiology and disease," Science **357**, eaaf4382 (2017).
[80]D. R. Scheff *et al.*, "Actin filament alignment causes mechanical hysteresis in cross-linked networks," Soft Matter **17**, 5499–5507 (2021).
[81]M. Preciado López *et al.*, "Chapter seventeen—*In vitro* reconstitution of dynamic microtubules interacting with actin filament networks," in *Methods in Enzymology*, edited by R. D. Vale (Academic Press, 2014), Vol. 540, pp. 301–320.
[82]S. Bhattacharjee, "DLS and zeta potential—What they are and what they are not?," J. Controlled Release **235**, 337–351 (2016).
[83]K. Guo, J. Shillcock, and R. Lipowsky, "Self-assembly of actin monomers into long filaments: Brownian dynamics simulations," J. Chem. Phys. **131**, 015102 (2009).